PCCP

ROYAL SOCIETY OF CHEMISTRY

PAPER

View Article Online
View Journal | View Issue

Cite this: *Phys. Chem. Chem. Phys.*, 2021, **23**, 10377

Interactions between butterfly-like prismatic dislocation loop pairs and planar defects in Ni_3Al†

Zhiwei Zhang,[ab] Qiang Fu,[c] Jun Wang,*[a] Rong Yang,[a] Pan Xiao,[a] Fujiu Ke[d] and Chunsheng Lu[e]

Received 18th February 2021,
Accepted 6th April 2021

DOI: 10.1039/d1cp00741f

rsc.li/pccp

Understanding the interactions between planar defects and complex dislocation structures in a material is of great significance to simplify its design. In this paper, we show that, from an atomistic perspective, by using molecular dynamics simulations on nanoindentations, a prismatic dislocation loop in Ni_3Al appears in pairs with a butterfly-like shape. The planar defects in Ni_3Al can effectively block the movement of the prismatic dislocation loop pairs and play a hardening role. Among the impediment factors, twinning boundaries are the strongest and antiphase boundaries are the weakest. Superlattice intrinsic and complex stacking faults have basically the same blocking effect. Furthermore, we systematically elucidate the hardening effects and interaction mechanisms between the prismatic dislocation loop pairs and planar defects. These findings provide novel insights into the nanostructured design of materials with excellent mechanical properties.

1. Introduction

As is known, alloying is a strategy for improving the performance of engineering materials. However, it is more dependent on resources and not conducive to recycling and re-utilization. In contrast, adjusting intrinsic defects to achieve the "plainification" of materials can sustainably enhance their properties.[1–4] Therefore, defect engineering, one of the key strategies of material design, has been utilized to develop advanced nanostructured materials.[5–8] Over the past several decades, nanoscale microstructural design has become an important research direction to further improve the performance of materials. Numerous experimental tests and computational simulations have been carried out in order to reveal the mechanical properties and deformation mechanisms of nanostructured materials. It has been shown that twinning boundaries can simultaneously enhance the strength and ductility of nanostructured face-centered-cubic (FCC) metallic materials.[9–12] Moreover, a stacking fault, another type of planar defect, can also effectively improve the strength and toughness of nanostructured hexagonal close-packed metals and other materials.[13–15] In addition, grain boundaries have long been proven to be a planar defect that can regulate the properties of materials.[16–18] However, the interactions between planar defects and dislocations are extremely complex in nanostructured materials. Thus, previous research studies were mainly focused on the interactions between a single edge/screw dislocation line and a twinning boundary or stacking fault.[19–21] The interaction mechanism between complex dislocations and planar defects remains unclear. To the best of our knowledge, studies on the interaction mechanisms between planar defects and complex dislocations are still lacking.

Recently, there has been increasing interest in the prismatic dislocation loop (PDL), which is fairly a complex dislocation assemblage. Its formation is believed to be the main mechanism of void growth in ductile materials and very important for irradiated materials.[22–24] The PDL composed of stacking faults and a variety of dislocations is movable in a crystalline structure, which can effectively contribute to its plastic behavior. It has been shown that PDLs were observed during indentation[25,26] and nanoindentation, with their nucleation mechanisms being well discussed.[27,28] However, the interactions between PDLs and planar defects have never been touched.

Single-crystal Ni_3Al, an intermetallic ordered alloy, has been widely applied in aerospace industries such as turbine blades and vanes in aircraft engines due to its potential corrosion, oxidation and creep resistance, high strength and good thermal properties.[29,30] Depending on the complexities of superlattice microstructures, there are four types of stable inherent planar defects in Ni_3Al, *e.g.*, twinning boundary, superlattice intrinsic

[a] *State Key Laboratory of Nonlinear Mechanics (LNM), Institute of Mechanics, Chinese Academy of Sciences, Beijing 100190, China. E-mail: wangjun@lnm.imech.ac.cn*
[b] *School of Engineering Science, University of Chinese Academy of Sciences, Beijing, 100049, China*
[c] *Aero Engine Academy of China, Beijing, 101304, China*
[d] *School of Physics, Beihang University, Beijing 100191, China*
[e] *School of Civil and Mechanical Engineering, Curtin University, Perth, WA 6845, Australia*

† Electronic supplementary information (ESI) available. See DOI: 10.1039/d1cp00741f

stacking fault, complex stacking fault and antiphase boundary.[31,32] This makes the deformation mechanism of Ni_3Al more complex than that of ordinary FCC metals. However, this also provides more microstructures to control and improve its mechanical properties. Studying the regulation mechanisms of these four main types of planar defects in Ni_3Al can contribute to a better understanding of the mechanical properties and microscopic deformation mechanisms of nanostructured Ni_3Al. Therefore, it is of interest to scrutinize the detailed mechanism of dislocation reactions between planar defects and PDLs in Ni_3Al.

In this paper, twinning boundary, superlattice intrinsic stacking fault, complex stacking fault and antiphase boundary are introduced into Ni_3Al to investigate whether such configurations could harden the Ni_3Al substrate in comparison with single-crystal Ni_3Al. For simplicity, we present the simulated indentation force and interfacial potential energy to describe the interaction process between PDL pairs and planar defects of Ni_3Al during indentation. This paper is organized as follows. In Section 2, the microstructures of planar defects in Ni_3Al and the adopted simulation methods are discussed. Section 3 is then dedicated to a detailed discussion on the interaction between PDLs and planar defects. The distinction of interactions between PDLs and various planar defects, and the hardening mechanism are discussed in Section 4. Finally, the main conclusions are given in Section 5.

2. Methods

2.1. Microstructures of planar defects in Ni_3Al

Single-crystal Ni_3Al displays an $L1_2$ crystal structure of an ordered derivative of FCC, with Al atoms at the cube corners and Ni atoms at the center of each face (see the inset in Fig. 1a). For the deformation in Ni_3Al, one stable dissociation of a $\langle 110 \rangle$ super-dislocation generates two $1/3\langle 112 \rangle$ Shockley super-partial dislocations bounded with a superlattice intrinsic stacking fault. The metastable dissociation of a $\langle 110 \rangle$ super-dislocation brings one $1/2\langle 110 \rangle$ super-partial and two $1/6\langle 112 \rangle$ Shockley partials bounded with a complex stacking fault. The other stable dissociation of dislocations is that a $\langle 110 \rangle$ super-dislocation dissociates into two $1/2\langle 110 \rangle$ super-partials bounded with an antiphase boundary on the (111) and (010) planes, respectively.[31–33]

Generally, in the case that atoms are displaced by $1/3\langle 112 \rangle$ displacement vectors, Al atoms are displaced to the same site but to a position corresponding to a different layer. Therefore, the stacking sequence is altered without the creation of any anti-site, which creates a superlattice intrinsic stacking fault. In the case that a displacement of $1/6\langle 112 \rangle$ is generated, Al atoms move to the anti-site and also to a position that corresponds to a different layer. In this process, a complex stacking fault is created. Whenever atoms on the (111) planes are displaced by the $1/2\langle 110 \rangle$ vector in the Ni_3Al configuration, Al atoms are displaced to the anti-site, generating antiphase boundary (111) defects (hereafter referred to as the antiphase boundary). Specifically, Ni_3Al models with planar defects of superlattice intrinsic stacking faults, complex stacking faults and antiphase boundaries are formed by shearing a (111) plane with $a/3[11\bar{2}]$ (111), $a/6[11\bar{2}]$ (111) and $a/2[101]$ $(\bar{1}11)$, with a being the lattice constant of Ni_3Al, respectively.[33,34] In addition, a twinning boundary is constructed by an anti-stacking order in contrast to that of single-crystal Ni_3Al at the two opposite sides of a (111) plane (see the insets in Fig. 1b–e).

2.2. Molecular dynamics simulations

Nanoindentations of Ni_3Al with planar defect models were simulated to investigate the hardening effects of planar defects by selecting a single-crystal Ni_3Al substrate as a reference. Fig. 1a shows the initial configuration of the single-crystal Ni_3Al substrate in the indentation simulation. All Ni_3Al substrates were created with a cubic shape of sizes $30 \times 30 \times 60$ nm^3 along the X-$[00\bar{1}]$, Y-$[1\bar{1}0]$ and Z-$[110]$ directions, containing $\sim$4 820 000 atoms (see Fig. 1a–e). A rhombic virtual plane indenter was used with a size of 3.5×2.6 nm^2 to produce pure PDL pairs so that the interactions can be quantified between them and a planar defect. During indentation, a periodic boundary condition was introduced in the Y-$[1\bar{1}0]$

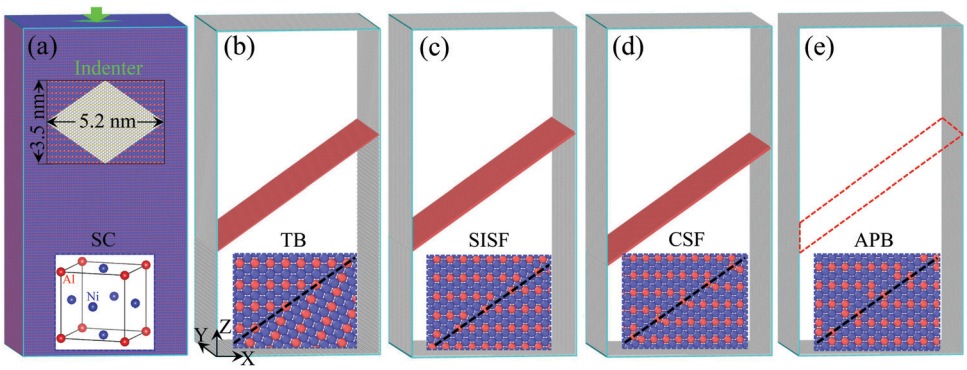

Fig. 1 (a) Sketch of the nanoindentation model for a single-crystal (SC) Ni_3Al substrate to generate prismatic dislocation loop pairs, and the nanostructured $L1_2$ Ni_3Al with planar defects of (b) twinning boundary (TB), (c) superlattice intrinsic stacking fault (SISF), (d) complex stacking fault (CSF) and (e) antiphase boundary (APB), where atoms are colored by common neighbor analysis with white and red representing the surface atoms and planar defects. FCC structures were removed for clarity in (b–e). The antiphase boundary in (e) is indicated by a red dashed box. The inset in (a) shows the three-dimensional structure of a Ni_3Al cell and the insets in (b–e) show their local enlarged structures.

crystallographic direction, while free boundary conditions were implemented along the other two directions to ensure that the surface interacted with the indenter is (110). In order to monitor the variations of the interfacial potential energy, both sides of planar defects with a thickness of ~0.5 nm were surveyed and defined as the "interfacial zone". Then, the potential energy per atom in an interfacial zone was computed and summed to obtain the interfacial potential energy. For comparison, the interfacial zone was also prefabricated at the corresponding position of the single-crystal Ni_3Al substrate. To avoid translation in the Z direction, all samples were restrained by an opposite body force distributed equally among the bottom atoms with a thickness of 1.0 nm. The value of the body force is precisely that of the load imposed by the indenter on (110) planes.

Atomistic simulations were performed by using the Large-scale Atomic/Molecular Massively Parallel Simulator.[35] The embedded-atom potential function for a Ni–Al system developed by Mishin[36] was taken to define the atomic interactions of Ni_3Al. In this function, the total energy, E, of a system can be described as

$$E = \sum_{\substack{i,j \\ i \neq j}} \phi_{\mathrm{EAM}}(r_{ij}) + \sum_i F(\overline{\rho_i}), \quad (1)$$

where $\varphi_{\mathrm{EAM}}(r_{ij})$ is the pair interaction energy represented as a function of the distance r_{ij} between atoms i and j, and F is the embedding energy of atom i, and $\overline{\rho_i}$ is the function of electron density, which is given by

$$\overline{\rho_i} = \sum_{i \neq j} f_j(r_{ij}), \quad (2)$$

where $f_j(r_{ij})$ is the electron density of atom j.

Simulations were carried out by integrating Newton's equations of motion for all atoms with a time step of 2 fs. At the start of simulations, initial configurations were energetically minimized by relaxing all samples for 20 ps. The temperature was controlled at 1 K during simulations to avoid thermal effects. The indentation speed and maximum indentation depth were 5 m s^{-1} and 5.0 nm, respectively. The dislocation types and structural formation under indentations were first recognized by calculating the number of common neighbors around an atom. Then, its discrepancy from a perfect crystalline lattice was employed to show the structural formation. Finally, Burgers vectors were obtained by building Burgers circuits around those atoms deviating from the perfect crystalline lattice.[37]

3. Results

3.1. Nucleation of PDL pairs in single-crystal Ni_3Al

A typical indentation force–depth curve of single-crystal Ni_3Al first undergoes an upward trend until the depth reaches 0.51 nm at which a PDL nucleates (see A in Fig. 2a). Under indentation, four 1/6⟨112⟩ Shockley dislocations are generated along the {111} slip plane and adhere to the lower surface of the substrate. With the four 1/6⟨112⟩ dislocations moving downward, two 1/3⟨100⟩ Hirth dislocations form at two opposite joints of

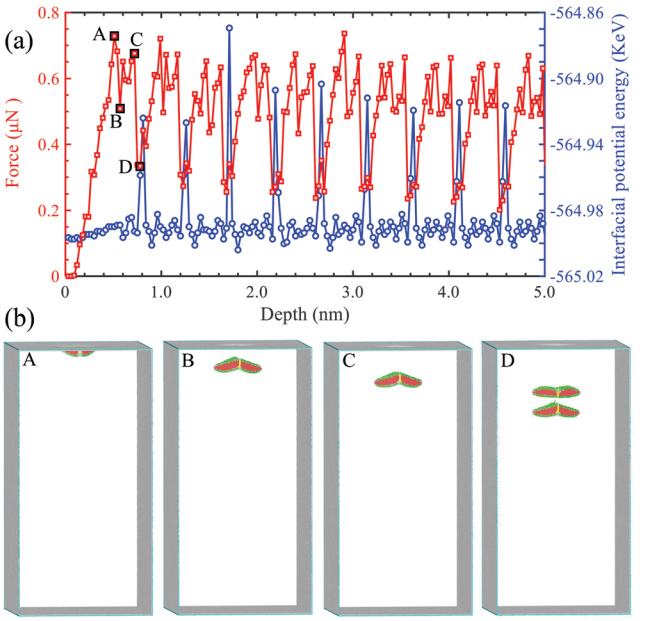

Fig. 2 (a) Typical indentation force/interfacial potential energy–depth relationships of single-crystal Ni_3Al. (b) Atomic configurations at points A–D in (a) correspond to various indentation depths of 0.51, 0.54, 0.57 and 0.72 nm, where atoms are colored by common neighbor and dislocation analysis.

the four 1/6⟨112⟩ dislocations. Meanwhile, two 1/6⟨110⟩ stair-rod dislocations appear at the other two opposite joints of the four 1/6⟨112⟩ dislocations. With the increase of depth, other four 1/6⟨112⟩ dislocations initiate at the surface of the substrate to link the already formed dislocation network. Thus, a PDL is established. As depth increases to 0.57 nm, this PDL separates from the surface of the substrate and the indentation force decreases to its local minimum (see B in Fig. 2b). After that, the indentation force increases again to its local maximum with the increase of depth to 0.69 nm, *i.e.*, C in Fig. 2b. At this point, the second PDL begins to nucleate. The separation of the second PDL from the surface witnesses a decrease of the indentation force to its local minimum once more at a depth of 0.72 nm (marked as D in Fig. 2a). After that, the two PDLs form a pair and move in coordination.

The microstructure of a PDL in Fig. 3 shows that it is composed of eight 1/6⟨112⟩ Shockley, two 1/3 ⟨100⟩ Hirth and two 1/6⟨110⟩ stair-rod dislocations. The 1/3⟨100⟩ Hirth and 1/6⟨110⟩ stair-rod dislocations act as stabilizing pinning locks, maintaining the structure of PDLs stable as they move inside the single-crystal Ni_3Al matrix. Further indentation reveals that PDLs always periodically appear in pairs and the corresponding indentation–depth curve experiences the same trend as that corresponding to the activities of the first PDL pair. The generating period of PDL pairs can be measured by the displacement, 0.3 nm, of the indenter between the two adjacent nucleating events of the PDL pairs and the speed of the indenter, 5 m s^{-1}. That is, PDL pairs are produced every 60 ps. The generation of PDL pairs in Ni_3Al differs by that in general FCC structural metal materials in which PDLs do not

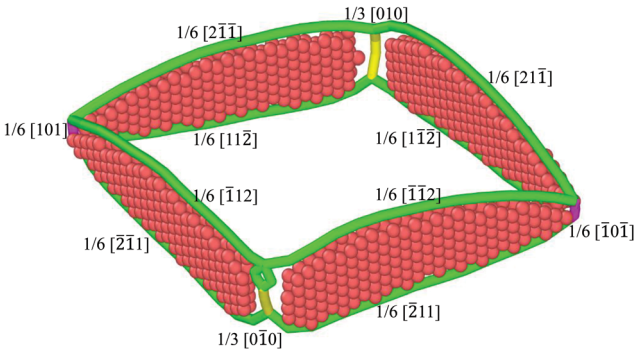

Fig. 3 Microstructure of a prismatic dislocation loop (PDL) is visualized by dislocation analysis, with green, purple and yellow lines indicating 1/6⟨112⟩ Shockley, 1/6⟨110⟩ stair-rod and 1/3⟨100⟩ Hirth dislocations, respectively. FCC structures were removed for clarity.

appear in pairs. This is because that the minimum Burgers vector in a $L1_2$ structure is two times of that in a FCC structure.[26]

Periodic activities of the PDL pairs are also reflected in the interface potential energy–depth curve. Specifically, as shown in Fig. 2a, when a PDL pair moves down along the slip plane and crosses the prefabricated interfacial zone, the interface potential energy produces a peak. After this, the pair passes through the interface area, and the potential energy returns to its original value. The period between the two successive peaks of the interface potential energy is also 60 ps. As the PDL pairs continue to nucleate and propagate, they finally cut through and disappear at the bottom of the substrate. The detailed dynamic evolution process can be found in Video S1 of the ESI.†

3.2. Interactions between PDL pairs and twinning boundaries

Outwardly, the indentation force–depth curve of the substrate with a twinning boundary can be divided into four stages *via* monitoring the indentation force, interfacial potential energy and dislocation activities (see Fig. 4a). In stage I, similar to the changing trend of the single-crystal Ni_3Al in Section 3.1 (see Fig. 2a), the force linearly increases with depth, suggesting a pure elastic deformation of the substrate. Then, it undergoes fluctuation, demonstrating the initiation and separation of the first PDL pair from the surface of the substrate. When the indentation depth reaches 0.78 nm (see the atomic pattern at A in Fig. 4b), the first PDL pair approaches the twinning boundary, so that the twinning boundary plane is subjected to an attractive force to generate stress concentration in areas directly below the PDL pair. In stage II, the first PDL pair oscillates up and down above the twinning boundary plane, and the corresponding interfacial potential energy also fluctuates violently. The atomic configuration corresponding to stage II can be seen in Fig. S1 (ESI†). In stage III, at an indentation depth of 1.32 nm, the first PDL pair contacts and reacts with the twinning boundary. At the same time, the second PDL pair also completes nucleation and moves downward (see the atomic pattern at B in Fig. 4b). Because the first PDL pair adheres to the twinning boundary plane, the interfacial potential energy

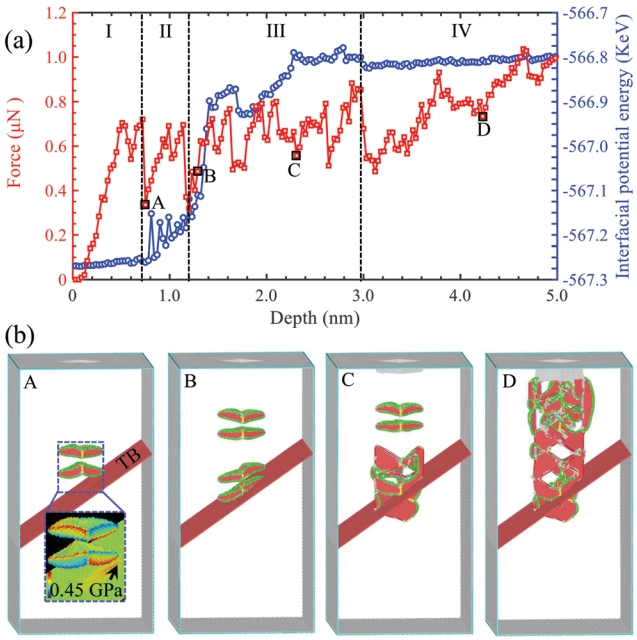

Fig. 4 (a) Indentation force/interfacial potential energy–depth relationships of Ni_3Al with a twinning boundary (TB), (b) atomic configurations at various indentation depths of 0.78, 1.32, 2.37 and 4.20 nm, where atoms are colored by common neighbor and dislocation analysis, with green, blue, purple, yellow and red lines indicating 1/6⟨112⟩ Shockley, 1/2⟨110⟩ perfect, 1/6⟨110⟩ stair-rod, 1/3⟨100⟩ Hirth, and other kinds of dislocations, respectively. The inset in (b) indicates a partially enlarged structure colored according to the shear stress τ_{yz}.

grows significantly (around B in Fig. 4a). As the indentation depth continues to increase, the twinning boundary plane reacts with the first PDL pair to produce the dislocation pinning lock, which blocks the movement of this pair. Meanwhile, more PDL pairs generated from the indentation surface continuously move downward and accumulate on the twinning boundary plane to pile up (see the atomic pattern at C in Fig. 4b). In this stage, the indentation force shows an increase in general although accompanied by fluctuation. However, the interfacial potential energy increases precipitously until it reaches stabilization. After that, the indentation depth exceeds 3 nm, that is, stage IV. The newly generated PDL pairs have piled up and merged above the twinning boundary plane, and finally collapsed by themselves (see the atomic pattern at D in Fig. 4b). At this stage, the indentation force keeps increasing but the interfacial potential energy maintains a stable value. The detailed interaction process between the PDL pairs and the twinning boundary during indentation can be seen in Video S2 and Fig. S2 of Section S1 in the ESI.†

3.3. Interactions between PDL pairs and other planar defects

In general, the interactions between planar defects and PDL pairs do not alter the structure of the latter although they suffer changes in shape. Details are given in Sections S2–S4 of the ESI.† For a superlattice intrinsic stacking fault, its indentation force, interfacial potential energy and microstructure evolution are shown in Fig. S3–S5 (ESI†). Briefly, when the PDL pairs interact with the superlattice intrinsic stacking fault, a small

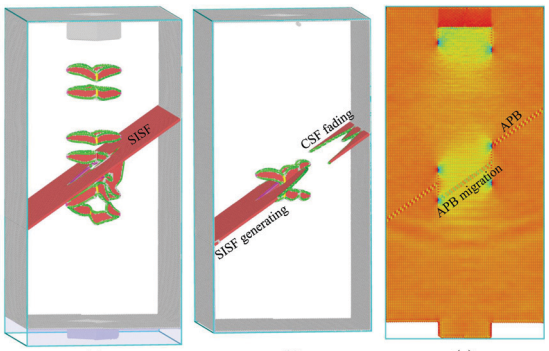

Fig. 5 Atomic configurations of Ni_3Al with planar defects of (a) superlattice intrinsic stacking fault (SISF), (b) complex stacking fault (CSF), and (c) antiphase boundary (APB), respectively, corresponding to various indentation depths of 4.53, 0.81 and 3.93 nm. Atoms in (a) and (b) are colored by common neighbor and dislocation analysis, with FCC structures being removed for clarity. Atoms in (c) are colored according to the stress σ_z.

amount of PDL pairs penetrated it adhere to its lower surface, resulting in the gradual increase of the interfacial potential energy. With the increase of the indentation depth, those PDL pairs adhered to the bottom surface of the superlattice intrinsic stacking fault also gradually detach and disappear from the bottom surface of the substrate (see Fig. 5a). The whole dynamic evolutionary process of interaction between the PDL pairs and the superlattice intrinsic stacking fault can be found in Video S3 of the ESI.†

For a complex stacking fault, with the increase of the indentation depth, the lower wing of the first PDL pair contacts the complex stacking fault plane, resulting in direct fading of their intersection, accompanied by the generation of new $1/6\langle 112\rangle$ Shockley dislocations at the edge of the faded region. Subsequently, the first PDL pair continues to move down, the complex stacking fault at the left of the PDL pair has faded and a layer of superlattice intrinsic stacking fault is generated. The newly generated superlattice intrinsic stacking fault expands along the original complex stacking fault plane before it is blocked by two $1/6\langle 110\rangle$ stair-rod dislocations as it arrives at the location of the first PDL pair. At the right side of the first PDL pair, the complex stacking fault also gradually fades with the propagation of the newly stimulated $1/6\langle 112\rangle$ Shockley dislocations on the original complex stacking fault plane (see Fig. 5b). Finally, the entire complex stacking fault is completely replaced by the newly generated superlattice intrinsic stacking fault. The indentation force, interfacial potential energy and microstructural evolution are shown in detail in Fig. S6 (ESI†). From Video S4 of the ESI,† the dislocation dynamic evolution can also be observed.

An antiphase boundary is a unique planar defect in Ni_3Al. The interactions between the antiphase boundary and the PDL pairs do not produce extra dislocations. However, a part of the antiphase boundary plane that interacted with the PDL pairs tends to migrate by an atomic layer after the penetration of half of the PDL pair. As shown in Fig. 5c, the partial antiphase boundary has migrated down by thirteen atomic layers, resulting from passing through of 6.5 PDL pairs. The indentation force, interfacial potential energy and microstructural evolution are shown in detail in Fig. S7 (ESI†). The dynamic interaction process between the PDL pairs and the antiphase boundary during indentation can be observed from Video S5 of the ESI.†

4. Discussion

4.1. Interactions between PDL pairs and planar defects

As mentioned above, the interactions between the PDL pairs and planar defects of Ni_3Al significantly depend on the types of planar defects. A twinning boundary has a superior blocking effect and can prevent the movement of the PDL pairs to the bottom of the substrate. This is because that the $\langle 110\rangle/\{111\}$ slip system changes by $90^\circ - \arccos\langle[110]\cdot[111]\rangle = 54.7^\circ$ with respect to the indentation direction below the twinning boundary plane. However, the $\langle 110\rangle/\{111\}$ slip system does not change at the two sides of the other planar defects. The interactions between the twinning boundary and the PDL pairs lead to the migration of the twinning boundary and the PDL pairs piling up on the twinning boundary surface. This also indirectly reflects that the twinning boundary has a good ability to prevent dislocation movement and absorb dislocations. That is, the twinning boundary can effectively improve the strength and toughness of nanostructured materials that are consistent with the experimental observations and simulations.[9–12] For example, based on nano-twinned metals, strengthening due to dislocation pile-up and softening induced by the migration of the twinning boundary were revealed by molecular dynamics simulations.[10] Moreover, such behaviors were also observed by Lu *et al.*[11] in experiments. It is of interest to point out that the impediment of the twinning boundary to PDL pairs is robust and none of them can get through.

For Ni_3Al with a planar defect of superlattice intrinsic stacking fault, as the indentation depth increases, most PDL pairs pass through the superlattice intrinsic stacking fault and disappear from the bottom of the substrate, just like the behavior of PDL pairs in single-crystal Ni_3Al. However, there is still a small amount of PDL pairs that adhere to the lower surface of the superlattice intrinsic stacking fault. This is the reason that superlattice intrinsic stacking fault falls behind the twinning boundary in the hardening effect. After the transformation of the complex stacking fault to a superlattice intrinsic stacking fault, the substrate with these two kinds of planar defects behaves almost the same under indentation. The discrepancy in their hardening effects is mainly attributed to their energetic stability. According to the analysis of first principles, the energy of a complex stacking fault is nearly two times over that of a superlattice intrinsic stacking fault,[38,39] so the stability of the former is weaker than that of the latter. This is the main reason why the former transforms into the latter as it interacts with the first PDL pair.

As another kind of planar defect, the antiphase boundary has the smallest blocking effect on the motion of the PDL pairs in comparison with the above three planar defects. The only

Table 1 Indentation properties of Ni_3Al with planar defects, where values in brackets are theoretical predictions of eqn (3)

Structures	Average indentation force (nN)	Average hardness (GPa)	Increment of hardness (GPa)	Impeding coefficient
Single crystal	300.2	33.0	—	—
Twinning boundary	454.7	50.0	17.0 [18.7]	1.00
Superlattice intrinsic stacking fault	355.1	39.0	6.0 [7.1]	0.38
Complex stacking fault	358.0	39.3	6.3 [7.1]	0.38
Antiphase boundary	309.5	34.0	1.0 [1.5]	0.08

contribution to hardening is the migration of the partial antiphase boundary. The migration originates from the flowing unique interaction as an antiphase boundary meets a PDL. On one hand, the movement of the leading partial of a PDL eliminates the preexisting antiphase boundary, and on the other hand, the trailing partial of this PDL regenerates this structure but with a distance of an atomic layer from its original position. This is just the same observed in the perfect $L1_2$ intermetallic compound.[40,41]

In general, it can be deduced from the modes of interaction between the PDL pairs and the four types of planar defects that the twinning boundary has the best impediment to the movement of the PDL pairs, followed by the superlattice intrinsic stacking fault and complex stacking fault, while the antiphase boundary is the weakest one. This is consistent with our previous research results.[42]

4.2. Hardening effects of planar defects

The average indentation force and hardness of the nanostructured Ni_3Al significantly depend on the types of planar defects, as summarized in Table 1. The relationships between the indentation force/hardness with various indentation depths can be seen in Fig. S8 (ESI†). It is shown that, hardening is achieved by planar defects such as twinning boundary, superlattice intrinsic stacking fault, complex stacking fault and antiphase boundary with a hardness of 50.0, 39.0, 39.3 and 34.0 GPa, respectively, compared with that, 33.0 GPa, of the single-crystal Ni_3Al substrate. The indentation force has a similar change trend. The indentation force of Ni_3Al with a twinning boundary is the largest, and the force of Ni_3Al with an antiphase boundary is slightly bigger than that of the single-crystal Ni_3Al substrate.

To explain the hardening effects of planar defects, we consider a PDL pair with mass M moving to a rigid interface with speed v. After interacting time t, it gains a momentum loss of α ($0 \leq \alpha \leq 1$), which is defined as the impeding coefficient. This parameter can be regarded as the proportion of adhering events as n PDL pairs meet an interface. Since all PDL pairs lose their momentums above the twinning boundary, the corresponding value of α is 1 for all 8 collisions. In contrast, a single crystal obtains a value of 0 due to the lack of blocking mechanisms. The values of α for the superlattice intrinsic and complex stacking faults are directly counted by the ratio, 3 of adhering events to 8 of total collisions, that is, α = 3/8. The value of α = 0.08 for an antiphase boundary is measured by the variations in displacements of 9 PDL pairs at both sides of the antiphase boundary with a fixed time interval. Thus, the increment of hardness ΔH can be described as

$$\Delta H = \alpha \frac{nMv}{tS}, \quad (3)$$

where S is the area of the indenter. The detailed formula derivation and determination of parameters can be seen in Section S5 of the ESI.† This equation theoretically predicts that the increments of hardness resulting from the twinning boundary, superlattice intrinsic stacking fault, complex stacking fault, and antiphase boundary are 18.7, 7.1, 7.1 and 1.5 GPa, respectively, which are slightly bigger than our molecular dynamics results (see Table 1). This is because the momentum loss of the PDL pairs does not contribute to the hardness entirely. A part of it has been consumed to fade or transform the planar defects, or to migrate the twinning and antiphase boundaries.

5. Conclusions

The interactions between PDL pairs and planar defects in nanostructured Ni_3Al have been investigated by generating perfect PDL pairs and constructing planar defects by nanoindentation of molecular dynamics simulations. It is shown that PDLs are always generated in pairs with a butterfly-like shape and hardening can be achieved by planar defects such as the twinning boundary, superlattice intrinsic stacking fault, complex stacking fault and antiphase boundary with a single crystal as a reference. The main conclusions can be summarized as follows:

(1) A twinning boundary exhibits a superior blocking effect, which completely prevents the movement of PDL pairs.

(2) Superlattice intrinsic and complex stacking faults have basically the same blocking ability, which is 3/8 of that of the twinning boundary.

(3) An antiphase boundary only offers a slight hardening effect due to its migration.

These findings provide new insights into a deep understanding of the interaction mechanisms between PDL pairs and planar defects in nanostructured intermetallic compounds with the $L1_2$ structure, especially Ni_3Al, and benefit their optimal design and wide applications in aerospace industries.

Data availability

The data that support the findings within this paper are available from the corresponding authors upon reasonable request.

Author contributions

Z. W. Zhang: conceptualization, investigation, methodology, data curation, writing – original draft, and writing – review and editing. Q. Fu: formal analysis. J. Wang: conceptualization, supervision, writing – review and editing, and funding acquisition. R. Yang: funding acquisition and writing – review and editing.

P. Xiao: conceptualization and funding acquisition. F. J. Ke: methodology. C. Lu: conceptualization and writing – review and editing.

Conflicts of interest

The authors declare that they have no known competing financial interests or personal relationships that could have appeared to influence the work reported in this paper.

Acknowledgements

This work has been supported by the National Natural Science Foundation of China (Grant No. 11772332 and 11790292), the Strategic Priority Research Program of the Chinese Academy of Sciences (Project No. XDB22040501), and the Opening Fund of State Key Laboratory of Nonlinear Mechanics. The simulations were performed on resources provided by the Pawsey Supercomputing Center with funding from the Australian Government and the Government of Western Australia, the ScGrid of Supercomputing Center, Computer Network Information Center of the Chinese Academy of Sciences, and the LNMGrid of the State Key Laboratory of Nonlinear Mechanics.

References

1 X. Y. Li and K. Lu, *Science*, 2019, **364**, 733–734.
2 I. A. Ovid'Ko, R. Z. Valiev and Y. T. Zhu, *Prog. Mater. Sci.*, 2018, **94**, 462–540.
3 X. W. Li, T. Shi, B. Li, X. C. Chen, C. W. Zhang, Z. G. Guo and Q. X. Zhang, *Mater. Des.*, 2019, **183**, 108152.
4 B. K. Reck and T. E. Graedel, *Science*, 2012, **337**, 690–695.
5 J. Su, D. Raabe and Z. M. Li, *Acta Mater.*, 2019, **163**, 40–54.
6 T. Chookajorn, H. A. Murdoch and C. A. Schuh, Design of stable nanocrystalline alloys, *Science*, 2012, **337**, 951–954.
7 P. Sathiyamoorthi and H. S. Kim, *Prog. Mater. Sci.*, 2020, 100709.
8 X. W. Li, J. S. Liang, T. Shi, D. N. Yang, X. C. Chen, C. W. Zhang, Z. H. Liu, D. Z. Liu and Q. X. Zhang, *Ceram. Int.*, 2020, **46**, 12911–12920.
9 Y. T. Zhu, X. Z. Liao and X. L. Wu, *Prog. Mater. Sci.*, 2012, **57**, 1–62.
10 X. Y. Li, Y. J. Wei, L. Lu, K. Lu and H. J. Gao, *Nature*, 2010, **464**, 877–880.
11 L. Lu, X. Chen, X. Huang and K. Lu, *Science*, 2009, **323**, 607–610.
12 Y. T. Zhu, J. Narayan, J. P. Hirth, S. Mahajan, X. L. Wu and X. Z. Liao, *Acta Mater.*, 2009, **57**, 3763–3770.
13 Q. M. Peng, B. C. Ge, H. Fu, Y. Sun, Q. Zu and J. Y. Huang, *Nanoscale*, 2018, **10**, 18028–18035.
14 B. Chen, J. Wang, Q. Gao, Y. J. Chen, X. Z. Liao, C. S. Lu, H. H. Tan, Y. W. Mai, J. Zou, S. P. Rinfer, H. J. Gao and C. Jagadish, *Nano Lett.*, 2013, **13**, 4369–4373.
15 J. Wang, Y. G. Shen, F. Song, F. J. Ke, Y. L. Bai and C. S. Lu, *Europhys. Lett.*, 2015, **110**, 36002.
16 M. A. Meyers, A. Mishra and D. J. Benson, *Prog. Mater. Sci.*, 2006, **51**, 427–556.
17 X. L. Wu, M. X. Yang, F. P. Yuan, G. L. Wu, Y. J. Wei, X. X. Huang and Y. T. Zhu, *Proc. Natl. Acad. Sci. U. S. A.*, 2015, **112**, 14501–14505.
18 M. Calcagnotto, Y. Adachi, D. Ponge and D. Raabe, *Acta Mater.*, 2011, **59**, 658–670.
19 Z. H. Jin, P. Gumbsch, K. Albe, E. Ma, K. Lu, H. Gleiter and H. Hahn, *Acta Mater.*, 2008, **56**, 1126–1135.
20 Z. H. Jin, P. Gumbsch, E. Ma, K. Albe, K. Lu, H. Hahn and H. Gleiter, *Scr. Mater.*, 2006, **54**, 1163–1168.
21 H. J. Wei and Y. G. Wei, *Mater. Sci. Eng., A*, 2012, **541**, 38–44.
22 H. Y. Yu, A. C. Cocks and E. Tarleton, *Scr. Mater.*, 2020, **189**, 112–116.
23 S. Lee, A. Vaid, J. Lm, B. Kim, A. Prakash, J. Guénolé, D. Kiener, E. Bitzek and S. H. Oh, *Nat. Commun.*, 2020, **11**, 2367.
24 H. G. Xiang, H. T. Li, T. Fu, C. Huang and X. H. Peng, *Acta Mater.*, 2017, **138**, 131–139.
25 S. Roy and D. Mordehai, *Acta Mater.*, 2017, **127**, 351–358.
26 C. Erel, G. Po, T. Crosby and N. Ghpniem, *Comput. Mater. Sci.*, 2017, **140**, 32–46.
27 S. Mishra, M. Meraj and S. Pal, *J. Mol. Model.*, 2018, **24**, 167.
28 S. S. Jiao, W. J. Tu, P. G. Zhang, W. Zhang, L. G. Qin, Z. M. Sun and J. Chen, *Comput. Mater. Sci.*, 2018, **143**, 384–390.
29 K. Xiong, H. M. Lu and J. F. Gu, *Comput. Mater. Sci.*, 2016, **115**, 214–226.
30 X. Y. Yang and W. Y. Hu, *J. Appl. Phys.*, 2014, **115**, 153507.
31 Y. F. Wen, J. Sun and J. Huang, *Trans. Nonferrous Met. Soc. China*, 2012, **22**, 661–664.
32 X. J. Gao, J. W. Wang, X. Z. Wu, R. Wang and Z. H. Jia, *Crystals*, 2018, **8**, 96.
33 X. X. Yu and C. Y. Wang, *Mater. Sci. Eng. A*, 2012, **539**, 38–41.
34 H. X. Xie, B. Liu and Y. Tao, *Modell. Simul. Mater. Sci. Eng.*, 2011, **19**, 065005.
35 S. Plimpton, *J. Comput. Phys.*, 1995, **117**, 1–19.
36 Y. Mishin, *Acta Mater.*, 2004, **52**, 1451–1467.
37 A. Stukowski, *Model. Simul. Mater. Sci. Eng.*, 2009, **18**, 015012.
38 L. L. Liu, X. Z. Wu, R. Wang, W. G. Li and Q. Liu, *Chin. Phys. B*, 2015, **24**, 077102.
39 J. Wang and H. Sehitoglu, *Intermetallics*, 2014, **52**, 20–31.
40 G. Inden, S. Bruns and H. Ackermann, *Philos. Mag.*, 1986, **53**, 87–100.
41 C. A. Becker, Y. Mishin and W. J. Boettinger, *J. Mater. Sci.*, 2008, **43**, 3873–3880.
42 Z. W. Zhang, Q. Fu, J. Wang, P. Xiao, F. J. Ke and C. S. Lu, *Comput. Mater. Sci.*, 2021, **188**, 110201.